Experimental investigation on the structural response of RC slabs subjected to combined fire and blast

Colombo, Matteo; Martinelli, Paolo; Arano, Assis; Øverli, Jan Arve; Hendriks, Max A.N.; Kanstad, Terje; di Prisco, Marco

DOI
10.1016/j.istruc.2021.02.029

Publication date
2021

Document Version
Final published version

Published in
Structures

Structures 31 (2021) 1017–1030

Contents lists available at ScienceDirect

Structures

journal homepage: www.elsevier.com/locate/structures

Experimental investigation on the structural response of RC slabs subjected to combined fire and blast

Matteo Colombo [a], Paolo Martinelli [a,*], Assis Arano [b], Jan Arve Øverli [b], Max A.N. Hendriks [b,c], Terje Kanstad [b], Marco di Prisco [a]

[a] Politecnico di Milano, Department of Civil and Environmental Engineering, Piazza L. da Vinci 32, 20133 Milan, Italy
[b] Norwegian University of Science and Technology, Department of Structural Engineering, NO-7491 Trondheim, Norway
[c] Technical University of Delft, Faculty of Civil Engineering and Geosciences, Stevinweg 1, Delft, Netherlands

ARTICLE INFO

Keywords:
Fire exposure
Blast loading
High temperatures
Shock tube
RC slabs
Fire-blast interaction

ABSTRACT

Reinforced concrete (RC) submerged floating tunnels (SFTs) represent a possible solution for crossing wide, deep fjords, and is considered for the E39 highway route along the Norwegian west coast. With regard to SFTs, the specific accidental scenario that is under investigation is the combined action of fire and subsequent internal explosion, as this is a crucial safety design condition for this type of structure. To assess the structural performance of reinforced concrete structures under combined fire and blast actions, gas burner equipment and a shock tube device were used to generate high temperature and blast loading, respectively, on RC circular slabs. A proper set of instruments consisting of thermocouples embedded in the specimens, accelerometers and ultrasonic pulse velocity (UPV) equipment made it possible to capture the behaviour of the slabs under the combined fire and blast actions and to distinguish the specific role of fire and blast. Simplified numerical tools such as an equivalent elastic single degree of freedom (SDOF) model and a linear elastic finite element (FE) model were used to interpret the experimental results. By considering all combinations of three fire exposure times and two shock waves, the effect of damage accumulation from a combined action of fire and subsequent internal explosion was mapped. A reliable benchmark for numerical models was obtained.

1. Introduction

Tunnels represent one of the most critical infrastructures in the whole transport network of Europe. Their fragility when exposed to exceptional events like fire and/or explosion is a crucial point in the robustness of a wider transport system, from damage of the infrastructure itself to a more far-reaching domino effect, propagating consequences over a wider region due to the tunnel closure. Tunnels are bottlenecks in transport networks that can threaten the overall robustness of the system, because the breakdown of those single components can lead to the complete collapse of the transportation infrastructure. From this point of view, a capacity design approach should be adopted to minimize the failure probability of the critical points.

Disastrous events that occurred in European road tunnels, such as those of the Mont Blanc Tunnel (1999), the Gotthard Tunnel (2001), the Tauern Tunnel (2002) and the Frejus Tunnel (2005), increased attention paid to safety issues in tunnels and underlined the importance of these infrastructures from human, economic and cultural points of views.

Fire has been regarded as the main physical threat in the design of a tunnel and a wide range of research activities including experimental tests, modelling methods and design approaches have been devoted to the investigation of this problem [1–15]. However, nowadays, fire cannot be regarded as the only extreme accidental action: recent terroristic attacks have raised the doubt that tunnel infrastructures can also be regarded as critical targets, not only for significant life losses, but also for the huge overall costs to society, that critical damage to this kind of infrastructure can induce. Over the last decade, several researchers started to examine the behaviour of tunnels (particularly metro tunnels) subjected to internal explosion encompassing both simplified and refined numerical models [16–25]. At present, there are no experimental studies reported in literature on the topic of tunnels subjected to internal blast loads.

The research presented in this paper concerns the preliminary design of the submerged-floating tunnel (SFT), or “Archimede bridge”, or

* Corresponding author at: Politecnico di Milano, Department of Civil and Environmental Engineering, Piazza L. da Vinci 32, 20133 Milan, Italy.
E-mail addresses: matteo.colombo@polimi.it (M. Colombo), paolo.martinelli@polimi.it (P. Martinelli), assis.arano@ntnu.no (A. Arano), jan.overli@ntnu.no (J.A. Øverli), max.hendriks@ntnu.no (M.A.N. Hendriks), terje.kanstad@ntnu.no (T. Kanstad), marco.diprisco@polimi.it (M. di Prisco).

https://doi.org/10.1016/j.istruc.2021.02.029
Received 17 November 2020; Received in revised form 12 January 2021; Accepted 11 February 2021
Available online 5 March 2021

Submerged Floating Tube Bridge (SFTB), that is planned for crossing Norwegian fjords. The Norwegian Public Roads Administration's Ferry-free coastal route E39 project aims to establish a coastal highway route, approximately 1100 km long, between Kristiansand and Trondheim without ferry connections. The wide, deep fjords along the Norwegian coast require new large structures to be built, and SFT is a realistic alternative [26].

The tunnel will be suspended approximately 30 m under the water's surface. The structure will comprise two tubes fixed to floating pontoons with a gap of approximately 250 m. This design allows ships to sail freely over the structure, while submarines can cross underneath it. With regard to SFTs, a specific accident scenario that is under investigation is the combined action of fire and subsequent internal explosion, as this is a crucial safety design condition for this structure. The tragic collision of two trucks on the Casalecchio (close to Bologna, Italy) junction of the A14 highway that occurred on August 6th 2018 can be regarded as an example of this kind of scenario: both trucks loaded with flammable materials (GPL and chemical solvents) triggered a chain of explosions that gutted the overpass, causing two deaths and 145 injuries. A recent study conducted by Kristoffersen et al. [23] analysed the response of SFTs with circular and rectangular cross-sections, subjected to internal explosion without fire using a finite element (FE) approach.

With reference to reinforced concrete (RC) structures, limited research is available in literature on the combined effects of fire and blast loads and is mostly confined to numerical studies. Kakogiannis et al. [27] and Pascualena et al. [28] reported the analysis of the blast bearing capacity of reinforced concrete hollow core slabs when they are subjected first to fire and then to a blast load. The blast response of the hollow core slab was assessed numerically in [28] and both numerically and experimentally in [27]. A numerical investigation into dynamic responses of RC columns subjected to fire and blast was proposed by Ruan et al. [29]. Zhai et al. [30] reported an experimental and numerical investigation of RC beams subjected to a blast after exposure to fire. A prestressed concrete panel was numerically evaluated under impact-blast-fire combined loading scenarios using an FE approach. Moving the attention to tunnels, the response behaviour of the tunnel lining under the action of vehicle impact and fire load has been numerically analysed [31]. A numerical simplified procedure was proposed by Colombo et al. [32] for the response behaviour of underground tunnels subjected to combined fire and internal explosion.

The work presented here aims to define a reliable benchmark for the numerical model that will be instrumental for the design of the tunnel under exceptional load conditions, by assessing the blast load-bearing resistance of RC slabs subjected to high temperatures. For this purpose, a comprehensive experimental program was carried out at Politecnico di Milano in conjunction with the Norwegian University of Science and Technology (NTNU), adopting a shock tube and gas burner equipment, able to apply a fire and blast sequence [33]. The work presented in this study is part of a larger research programme in which static slab tests and material tests, have been performed for further understanding of the slab's behaviour [34].

The structural response of RC circular slabs subjected to shock wave load conditions was investigated in residual conditions, after being exposed to a fire curve. According to [35], a hydrocarbon fire curve, typical of tunnel designing, was first applied to five specimens. Two fire exposure times were considered (t = 60 and 120 min) in addition to the reference case (t = 0 min). The same guideline [35] indicates t = 120 min as the fire exposure time in the case of a tunnel that is a primary structure, with truck/tanker type traffic.

Two different shock wave loading conditions were taken into account: a "low pressure" condition (LP) characterized by an incident shock wave travelling at a velocity about 1.5 Mach and a maximum reflected pressure of about 400 kPa, and a "High Pressure" condition (HP) characterized by an incident shock wave travelling at a velocity of about 2 Mach and a maximum reflected pressure of 1100 kPa.

Thermocouples embedded in the specimens made it possible to measure the temperature distribution through the thickness of the specimens during the fire application, whilst accelerometers, applied to the back of the slab during the shock tube tests, made it possible to measure the acceleration at several points of the specimens. Moreover, ultrasonic pulse velocity (UPV) measurements were acquired, before and after the fire tests and also after the shock tube tests, in order to quantify the decrease of the cross-section stiffness caused by both the fire exposure and the shock wave application.

Table 1
Summary of the experimental programme.

Specimen ID	UPV test	fire exposure			blast test	
		0 min	60 min	120 min	low pressure	high pressure
LP0	Y	Y	–	–	Y	–
LP60	Y	–	Y	–	Y	–
LP120	Y	–	–	Y	Y	–
HP0	Y	Y	–	–	–	Y
HP60	Y	–	Y	–	–	Y
HP120-1	Y	–	–	Y	–	Y
HP120-2	Y	–	–	Y	–	Y

2. Experimental programme

In this work, RC circular slabs were subjected to combined fire and shock wave loads. An overview of the whole experimental programme is presented in Section 2.1. A description of the materials composing the specimens (i.e. concrete and steel) is given in Section 2.2. The specimen's geometry and the instrumentation are presented in Section 2.3.

2.1. Test programme

In total seven specimens were tested in this study, of which five were tested under combined fire and shock wave loads. Two specimens were tested under blast conditions only. Table 1 summarizes the whole set of tests performed. In all the tests, exposure to fire (if applied) always preceded the blast load.

The experimental tests differ in terms of the reflected pressure history applied to the specimens and the time exposure at the fire curve eventually applied before the blast. Three tests, hereafter indicated as the low pressure tests, are characterised by an average peak pressure of 370 kPa and an average specific impulse of 3386 kPa × ms. The other four tests, hereafter indicated as the high pressure experiments, are characterised by an average peak pressure of 1111 kPa and an average specific impulse of 6241 kPa × ms. This study considers two different fire exposure times (t = 60 min and t = 120 min), in addition to the non-heated condition (t = 0 min). An abbreviation is used to indicate different tests that correspond to different specimens (for example HP120-1): LP or HP at the beginning of the abbreviation stand for low and high pressure tests, 0, 60 and 120 stand for the exposure time in minutes where 0 means that specimen was not exposed to fire, while the eventual ascending number at the end of the abbreviation identifies nominally identical specimens.

In all the tests, direct UPV measurements were performed before and after the fire tests and before and after the blast tests in order to quantify the internal damage produced by the combined effect of thermal exposure and blast load through the thickness of the specimen.

2.2. Materials

2.2.1. Concrete

A detailed and comprehensive discussion of the mechanical properties of the concrete used for the RC slabs is given in [34]. Mechanical properties of concrete were evaluated at ambient and high temperatures. Only the main points of interest are summarized in the following description.

Table 2
Concrete mix design.

Component	Content (kg/m^3)
CEM II/B-M 42.5R	223.40
CEM II/A-V 42.5 N	193.33
Silica fume	12.89
Water	174.13
Aggregate 8–16	754.95
Aggregate 0–8	1026.48
Acrylic superplasticizer	3.06
Set-retarding admixture	0.64
Polypropylene fibres	1.00

The concrete mix design ordered as a C45/55 grade is listed in Table 2. The concrete compressive strength (f_c) measured on cylinders (D = 100 mm and H = 200 mm) was equal to 73 MPa. The concrete cylinders were demoulded 24 h after casting, cured in water for 28 days, and rested for five/six months at 20 °C in a lab environment. The density (ρ) at 28 days was equal to 2370 kg/m^3. The concrete has a water-cement ratio (w/c) of 0.42, and a maximum aggregate size (d_{max}) of 16 mm. The siliceous aggregates were composed of granite, gneiss, sandstone and siltstone. Polypropylene microfibres were also added into the mix (1 kg/m^3) to prevent explosive spalling.

A set of quasi-static concrete tests, namely uniaxial compression test (UCT) and uniaxial direct tensile test (UTT) was carried out to assess the mechanical material properties of concrete at four different temperatures. Twelve standard cylinders (100 × 200 mm) were tested in uniaxial compression, measuring the modulus of elasticity as indicated in [36] and the compressive strength. Three nominally identical specimens were tested at different temperature levels (20, 200, 400, and 600 °C), in residual conditions. Eight cylinders (100 × 100 mm) were tested in uniaxial tension with hinged end-platens by controlling the crack opening displacement (COD). Two nominally identical specimens were tested in residual conditions at different temperature levels (20, 200, 400, and 600 °C). Further details on the material test set-up, specimen sizes and instrumentation can be found in [34].

The average modulus of elasticity from the three tests at 20 °C, and its standard deviation were equal to $E_{c,20}$ = 27609 ± 829 MPa. A significant decrease in the modulus of elasticity in concrete subjected to high temperature was observed. On average, from 20 to 200 °C, the modulus slightly reduces until 0.90$E_{c,20}$. Between 200–400 °C and 400–600 °C, the material suffers a faster reduction, reaching 0.50$E_{c,20}$ and 0.20$E_{c,20}$, respectively.

The average compressive peak strength from the three tests at 20 °C, and its standard deviation were equal to $f_{c,20}$ = 73.00 ± 2.44 MPa. The compressive strength of concrete was significantly reduced due to the exposure to elevated temperatures, with a trend similar to that observed for the modulus of elasticity. After exposure to elevated temperatures, the residual peak strength decreases to approximately 0.90$f_{c,20}$ after 200 °C, 0.50$f_{c,20}$ after 400 °C, and 0.30$f_{c,20}$ after 600 °C.

The average peak tensile strength from the two tests at 20 °C, and its standard deviation were equal to $f_{ct,20}$ = 3.62 ± 0.56 MPa. The maximum stress reached at 200 °C is about 20% higher than the maximum stress at 20 °C. Above 200 °C, the residual peak tensile strength significantly decreases to approximately 0.70$f_{ct,20}$ for 400 °C and 0.30$f_{ct,20}$ for 600 °C. Complete stress–strain and stress-COD curves were measured during the UCTs and UTTs, in addition to peak compressive strength and peak tensile strength, but are omitted here for the sake of brevity. A detailed and comprehensive discussion of the mechanical properties of concrete exposed to high temperatures is given in [34].

2.2.2. Steel

Traditional B450 steel with Ø6 mm rebars were used to prepare the RC circular slabs. Eight steel reinforcing bars were tested in uniaxial tension according to [37], using an INSTRON machine with a maximum capacity of 200 kN. The tests were carried out under displacement control by means of a high-accuracy transducer, with a gauge length of 50 mm, placed at the central part measuring the elongation of the rebar until it reached 2%. An internal transducer of the machine was then used to follow the test until complete failure of the specimen. Two nominally identical specimens were tested, in residual conditions at different temperature levels (20, 200, 400, and 600 °C). By controlling the displacement, complete stress–strain curves were measured during the tests, in addition to yielding and ultimate strengths. After the tests, the elongation at failure was measured according to [37]. The average yielding strength for the steel rebar at room temperature is $f_{y,20}$ = 500.85 MPa. The average ultimate strength and strain at room temperature are $f_{t,20}$ = 648.77 MPa and $\varepsilon_{su,20}$ = 0.328, respectively. The mechanical properties at high temperatures experienced a strong recovery during the cooling phase. The yielding and ultimate strength after exposure to 600 °C were very similar to those for the non-heated specimens.

2.3. Specimen geometry and instrumentation

The slab specimens consist of reinforced concrete circular slabs, 70 mm thick, with a diameter of 690 mm. Two layers of bi-directional reinforcement (Ø6/60 mm both in x and y direction) were positioned as shown in Fig. 1. A net concrete cover of 10 mm was used. The specimen sizes are detailed in Fig. 1.

The specimen's geometry was mainly dictated by the dimensions of the shock tube equipment. In addition, the thickness and reinforcement ratio were determined in order to ensure a linear elastic behaviour of the slab under the reference load conditions (test LP0). An elastic analytical computation of the slab [38], considering not thermally damaged

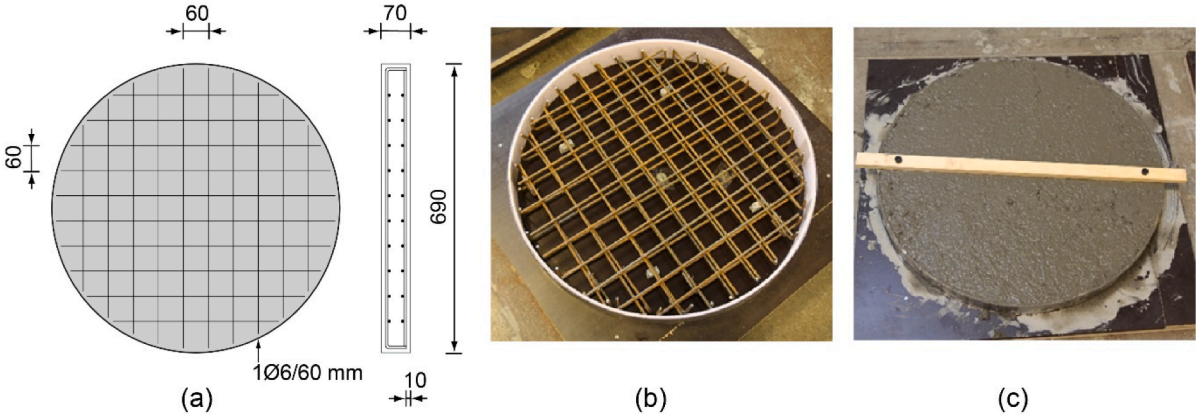

Fig. 1. Reinforced concrete slab specimen: (a) specimen size, (b) mould used to cast the slab and (c) view of the cast slab (units: mm).

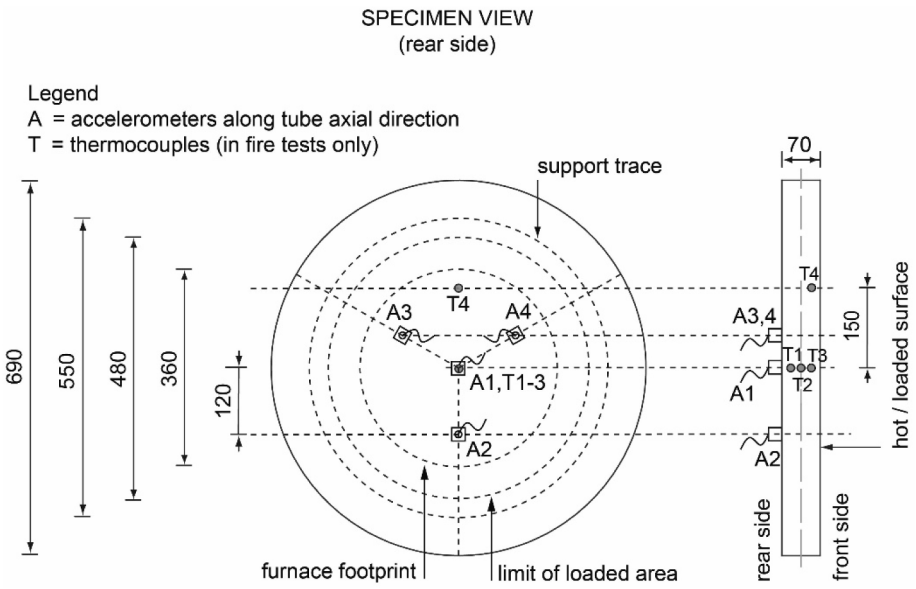

Fig. 2. Instrumentation installed on the specimen (units: mm).

material, provides a pressure corresponding to the first cracking (p_{cr}) in static condition equal to 400 kPa, while the ultimate pressure (p_u) computed according to a yield line approach [39] for static condition is equal to 1100 kPa.

The specimen's acceleration along the shock tube axis (out-of-plane slab acceleration) was measured by means of four ICP (Integrate Circuit Piezoelectric) accelerometers: one (A1) placed at the specimen's centre and the other three (A2–A4) placed at relative angular positions of 120° at 120 mm from the specimen's centre (Fig. 2). A fifth accelerometer (A5) was mounted on the shock tube at the end of the driven chamber to record the axial accelerations of the device (Fig. 6 and Fig. 7b). The accelerometer characteristics are: a quartz sensing element with a measuring range of ±500 g pk (peak acceleration), a band width larger than 10 kHz, a broadband resolution of 0.005 g rms (root mean square) and a resonant frequency higher than 70 kHz.

A set of three ICP dynamic pressure sensors was positioned along the tube's axis as indicated in Fig. 6. The pressure sensors (PT1-PT3) have a quartz sensing element with a full-scale pressure of 6.9 MPa, a sensitivity of 0.7 mV/kPa, a rise time lower than 1 μs and a resonant frequency higher than 500 kHz. The signal conditioning for both accelerometers and pressure sensors mounted on the shock tube (see Section 3.3 for its description) is performed with an ICP signal conditioner with gain equal to one, a bandwidth equal to 10 kHz and a broadband electrical noise equal to 3.5 μV rms. All channels are acquired by means of the same data acquisition system with 56 parallel channels with the maximum sampling rate of 3 MS/s per channel and a 14-bit resolution. The data acquisition for all the channels is triggered by the signal of the pressure sensor PT1 placed at a distance of 2250 mm from the driven end flange: when the shock wave goes through its position, the system starts acquiring data with a sampling rate of 1 MS/s.

Specimens exposed to high temperatures were instrumented with four thermocouples each. Type-K chromel/alumel thermocouples (0.91 mm thick) were installed during fabrication at three different depths in the specimen. Thermocouples T1-T3 were located at the centre of the specimen at 54, 35 and 16 mm from the "hot surface", respectively, for measuring the concrete temperature through the thickness. Thermocouple T4 was located at 150 mm from the centre along the radial direction at a depth of 16 mm from the "hot surface" (see Fig. 2).

3. Description of slab tests

The tests were conducted according to the following sequence: (a) application of UPV tests on virgin specimen, (b) application of the fire curve with exposure time equal to t = 60 min or t = 120 min, (c) UPV measurements for evaluation of fire damage, (d) application of low or high pressure blast tests and (e) UPV measurements for the assessment of combined fire and blast damage. Tests where high-temperature exposure was not applied (t = 0 min) served as reference tests; in these cases phases (b) and (c) were not applied. The description of UPV measurements, fire tests and blast tests is given in Sections 3.1–3.3.

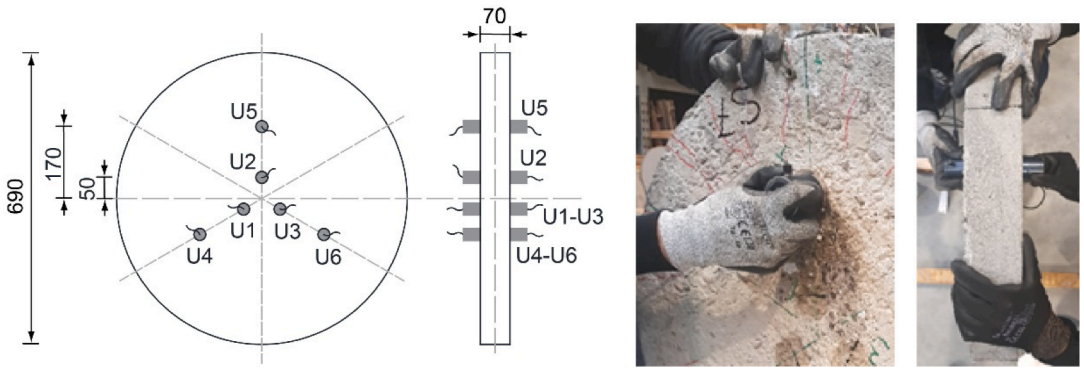

Fig. 3. Direct UPV measurements on RC slab specimen (units: mm).

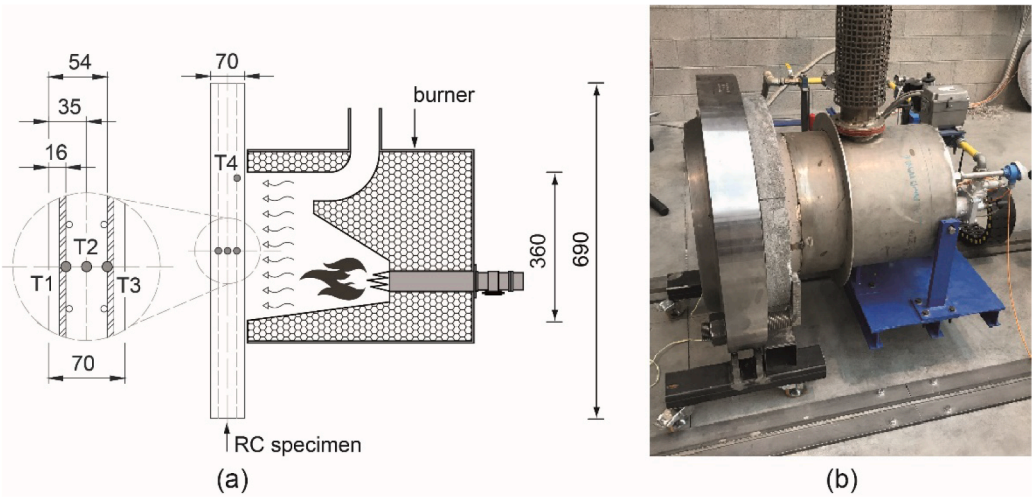

Fig. 4. Fire curve application: (a) schematic view of the burner equipment and (b) picture of the burner and of the specimen ready for the fire test (units: mm).

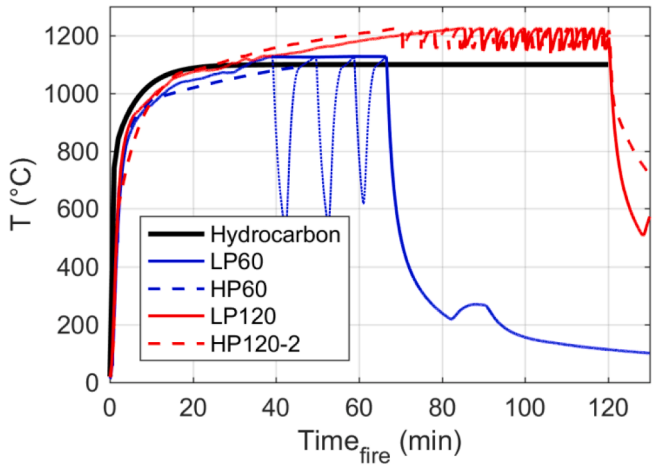

Fig. 5. Recorded and target fire curves.

3.1. UPV measurements

Direct UPV measurements [40] were carried out on the specimens before and after the fire and blast tests. The aim of these measurements was to quantify the internal damage produced by the thermal exposure and by the blast load through the thickness of each specimen. The emitting and receiving probes were placed on opposite specimen faces since a direct UPV method was adopted. Six points were monitored: points U1-U3 were located at a distance of 50 mm from the specimen's centre, whereas points U4-U6 were located at a distance of 170 mm (see Fig. 3). Gel was used to avoid air between the transducer and the specimen's surface.

3.2. Fire exposure

The fire curve was applied to the specimens by means of a gas burner. The burner equipment comprises a nozzle mix burner in which gas and air are mixed at the point of discharge. The burner is mounted by means of a proper flange to a chamber in which the burning process takes place. The chamber is designed to allow proper smoke evacuation and it is closed on one side by the specimen itself in order to heat the specimen's surface. A hydrocarbon curve [14], typical of accidents in tunnels, was applied on one face of the specimen (the free surface during casting) on a circular area with a diameter equal to 360 mm (Fig. 4). A thermal sensor installed inside the burner makes it possible to automatically regulate the intensity of the flame to achieve the desired temperature vs time curve (i.e. fire curve). Two different high temperature exposure times, t = 60 min and t = 120 min, were considered. The fire curves recorded during the fire tests are shown in Fig. 5 and compared with the target hydrocarbon fire curve. The specimens were allowed to expand freely due to increase of temperature during the test. Once the desired exposure time was reached, the burner was turned off and the specimens cooled naturally in the free laboratory environment. During the LP60 test there was a problem in following the target temperature. The problem was solved during the other tests and did not have any impact on the results that are presented in Section 4.

All specimens subjected to the fire curve were instrumented with four thermocouples for measuring the concrete temperature through the thickness (see Section 2.3 for the description of the instrumentation). Despite the addition of polypropylene microfibers in the concrete matrix, minor explosive spalling occurred during the first minutes of all the tests subjected to fire exposure. Nevertheless, this phenomenon was limited to a small region of the specimen and with a maximum depth close to the concrete cover (c = 10 mm). The region characterized by the spalling phenomenon is highlighted as a grey region in Fig. 13.

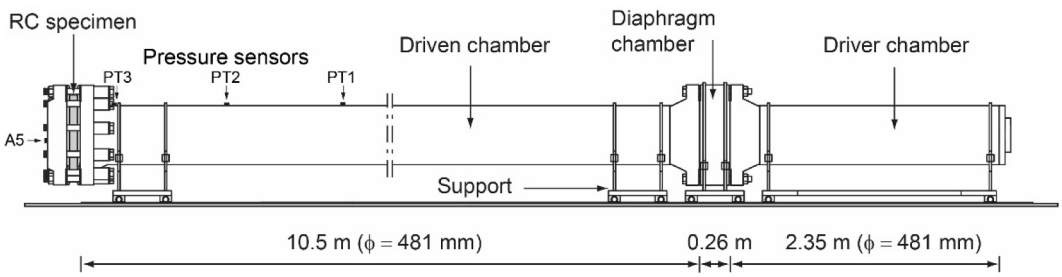

Fig. 6. Schematic view of the shock tube.

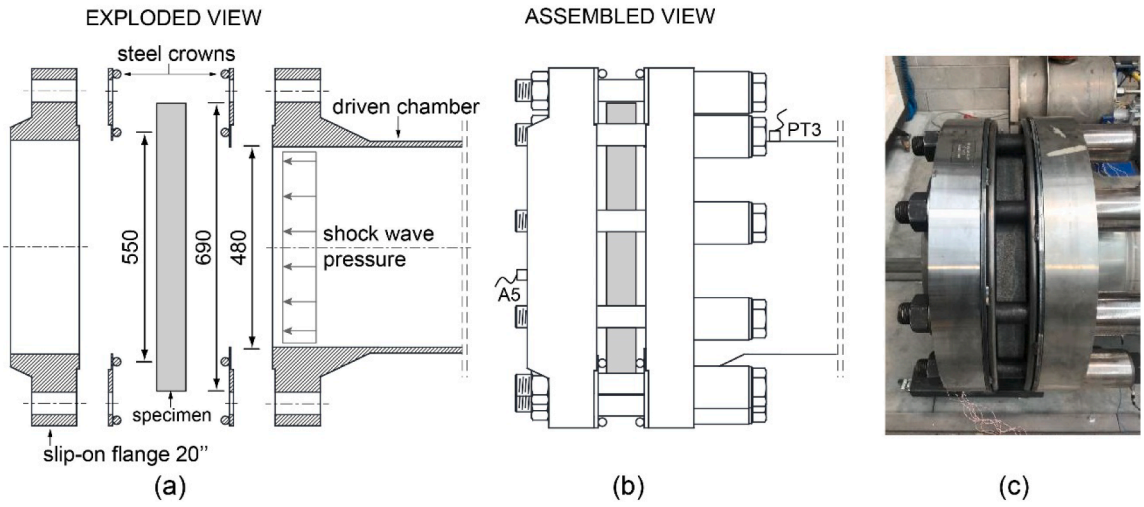

Fig. 7. Details of the test set-up area: (a) exploded view, (b) assembled view and (c) picture in the assembled configuration.

3.3. Blast tests

The blast tests were carried out at Politecnico di Milano by adopting a double diaphragm shock tube facility. The shock tube was used as blast simulator; the idea to use shock tubes to simulate blast loading on structures is not new and this technique was developed to reproduce blast waves nearly identical to those obtained in live explosive tests [41,42]. Examples of the use of shock tubes to analyse the dynamic behaviour of concrete slabs and RC slabs according to several boundary conditions, like simply supported/clamped or resting on the ground can be found in [43–45].

The shock tube was originally adopted to investigate the behaviour of underground tunnel linings under blast conditions [45,46] through the use of an ad-hoc chamber designed to investigate soil-structure interaction. The shock tube was easily adapted to study plates under blast loads with different boundary conditions by changing the end chamber. The shock tube is able to produce a high pressure loading range, with a maximum reflected target pressure of about 3000 kPa. A detailed description of all the shock tube's components can be found in [33], while a comprehensive discussion on the shock tube's performance is given in [47]; only the main points of interest are summarized below.

Fig. 6 shows a schematic layout of the shock tube device in the assembled configuration. It consists of three chambers that can move on a linear guide system: the driver chamber, the diaphragm chamber (i.e. firing section or buffer chamber) and the driven chamber. The test area in which the specimen is fixed is placed at the end of the driven chamber. The tests were carried out using pressurized helium inside the driver and buffer chambers, and air at ambient condition in the driven chamber.

Driver, buffer and driven chambers have a length of 2.35, 0.26 and 10.5 m, respectively, thus resulting in a total shock tube length, excluding the test area, of 13.11 m. The driver and driven chambers have a 13.5 mm thick wall, while the buffer chamber has an external diameter of 857 mm that corresponds to the maximum diameter of the flange welded on the driver and driven ends; for all three chambers the internal diameter is equal to 481 mm.

The firing mechanism is activated when the two scored steel diaphragms that separate the buffer chamber from the driver and driven chambers fail. The diaphragms' failure is obtained by a differential pressure created between the driver/buffer and buffer/driven chambers. During the failure of diaphragms four petals form and the rapid propagation of the pressurized gas into the driven chamber occurs leading to the creation of a shock wave.

A picture of the test set-up area is shown in Fig. 7. The equipment used to fix the specimen consists of two steel crowns and a steel reaction flange (see Fig. 7a). The specimens were placed between two steel crowns specifically designed to guarantee a bilateral simply supported condition. The reaction end flange, consisting of a slip-on flange of 20″, was connected to the driven end flange using ten M52 bolts. An exploded view of the test set-up area highlighting all the components is shown in Fig. 7a, while an assembled view of the test set-up area is shown in Fig. 7b-c.

Table 3
Shock wave characteristics.

Specimen ID	P_{peak} (kPa)	i_e^+ (kPa × ms)	t^+ (ms)	v_s (m/s)
LP0	339.1	3430	33.2	502
LP60	393.6	3451	39.7	500
LP120	376.3	3278	29.2	502
HP0	1090	6255	17.5	652
HP60	–	–	–	–
HP120-1	1118	6288	17.7	674
HP120-2	1126	6181	16.9	714

Mounting pressure sensors on a test sample to measure the load is not an easily practicable solution. Nevertheless, if deformations in the concrete slabs are small, the data from the sensor closest to the specimen face (sensor PT3) will provide a good approximation of the load that the concrete slabs experience.

Table 3 summarizes the main properties that characterize the shock wave for each test: the peak pressure (P_{peak}), the positive specific impulse (i_e^+) the duration of the positive specific impulse (t^+), and the shock wave velocity (v_s). The latter was calculated using the data from sensors PT1-PT3. The pressure time histories for all the blast tests recorded by the transducer closest to the specimen (sensor PT3 in Fig. 6) are shown in Fig. 8. It is important to point out that the reflected pressure histories applied to the specimens are very repeatable. This means that the change in stiffness of the specimens due to fire application does not lead to any significant contribution to the fluid–structure interaction phenomenon and therefore the mechanical problem can be considered uncoupled by shock wave propagation.

A problem occurred during test HP60 that prevented the correct recording of transducers PT1-PT3. Nevertheless, the high repeatability of these tests, clearly visible in Fig. 8, allows the HP60 test results to be used as well.

4. Test results

This section describes the main results obtained in the experimental investigation. Fig. 9 shows the evolution of temperatures, recorded by

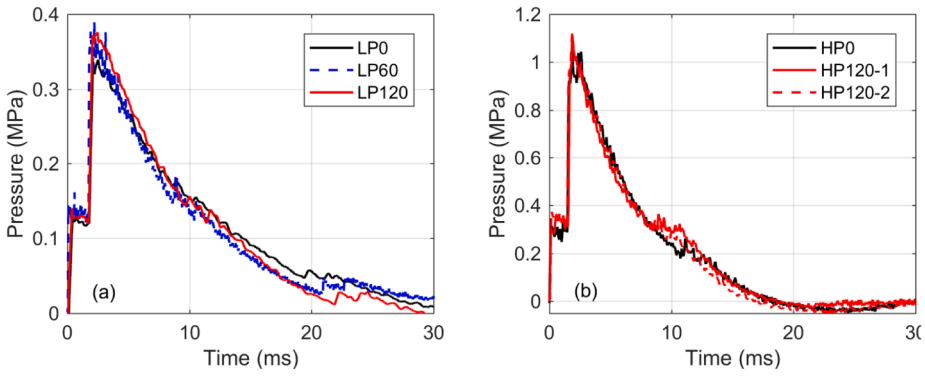

Fig. 8. Pressure–time histories for sensor PT3 in shock tube tests.

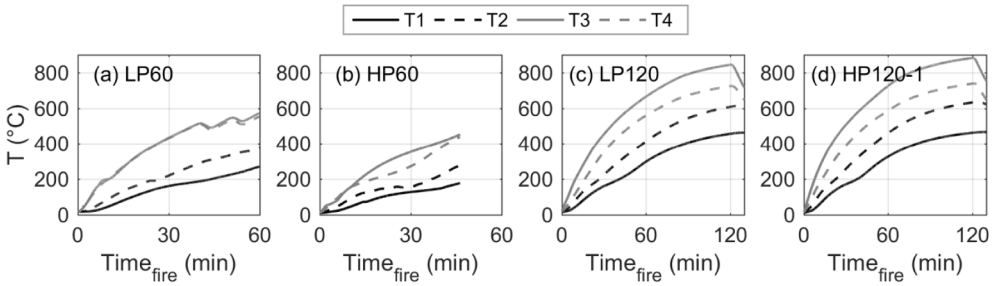

Fig. 9. Evolution of temperatures vs fire exposure time: (a) test LP60, (b) test HP 60, (c) test LP120 and (d) HP120-1.

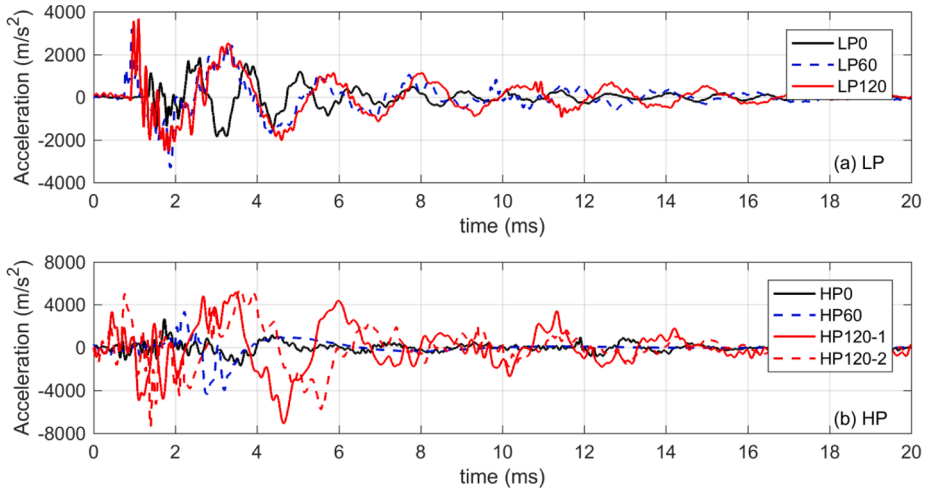

Fig. 10. Axial central specimen accelerations A1: (a) tests LP0, LP60, LP120 and (b) tests HP0, HP60, HP120-1, HP120-2.

thermocouples T1-T4, as the fire exposure time varies. Clearly, the highest temperature is read by thermocouple T3 that is closest to the burner (see Fig. 4). In specimens LP60 and HP60 (Fig. 9a-b), exposed to high temperature for a time of 60 min, the maximum temperature reached is about 600 °C, while the temperature on the specimen side not exposed to the fire is about 250 °C. Looking at specimens LP120 and HP120-1 (Fig. 9c-d) both characterized by a fire exposure time of 120 min, the maximum temperature reached is about 900 °C, while the temperature on the specimen side not exposed to the fire is about 450 °C. Although the fire curve was correctly applied to the HP60 specimen, a problem in data acquisition occurred in this test after approximately 45 min of fire exposure (Fig. 9b) and therefore the final data was lost.

The central accelerations of the specimens are compared in Fig. 10 for all the experimental tests. Fig. 10a and Fig. 10b compare low pressure (LP) and high pressure (HP) tests respectively, exposed to different fire exposure times (0, 60, 120 min). The influence of fire exposure time on the acceleration response of the specimens is illustrated and the elongation of the fundamental period of the specimens exposed to fire is clearly visible compared to the specimens not subjected to fire exposure. While for LP tests the exposure to fire modifies the frequency content of the response without significantly altering the maximum accelerations, in the HP tests the exposure to fire involves both a modification of the frequency content and an increase in the amplitude of the accelerations, thus indicating that the interaction between fire and blast is more pronounced.

When examining the frequency content of the recorded signals, it is important to remember that the shock tube is deformable and not fixed to the ground but can be moved on a linear guide system. For this reason, the axial acceleration of the tube was recorded during the tests using accelerometer A5 in order to distinguish the frequency content of the

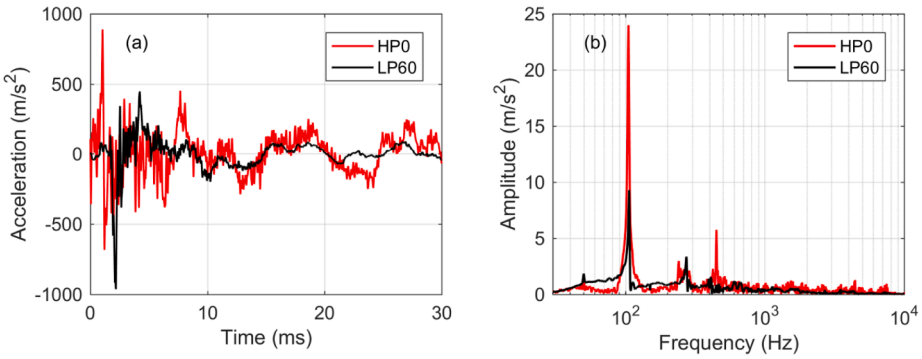

Fig. 11. (a) Shock tube axial acceleration A5 for tests HP0 and LP60 and (b) corresponding frequency spectrum.

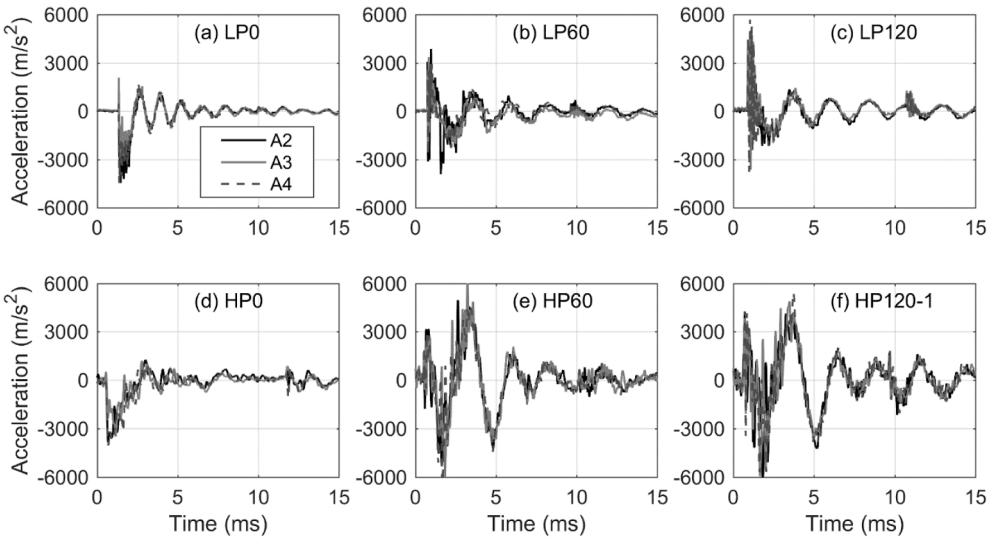

Fig. 12. Axial specimen accelerations A2-A4: (a) test LP0, (b) test LP60, (c) test LP120, (d) test HP0, (e) test HP60 and (f) HP120-1.

shock tube from the frequency content associated with the response of the specimens. The shock tube axial accelerations (A5) for tests HP0 and LP60, taken as an example, are shown in Fig. 11 together with the corresponding frequency spectrum. The main frequency associated with the axial movement of the tube is clearly visible in Fig. 11b and is equal to about 100 Hz.

Fig. 12 reports the results of the three accelerometers (A2–A4) placed at 120° in relation to each other on the specimens. The specimens' responses are characterised by an elevated symmetry. While this result was to be expected since the specimens are circular symmetric in terms of geometry and load, on the other hand the planarity of the shock wave impacting the specimens is confirmed. It is also interesting to note that the symmetry in the response is also preserved in the specimens exposed to the fire and which have therefore suffered damage (Fig. 12b-c-e-f). In fact, the presence of spalling is limited to small regions and even where it affects the symmetry of the specimen's geometry, it does not play a significant role on the symmetry of the specimens' response.

Fig. 13 shows front and rear crack patterns for all the tests with the exception of the LP0 test where no cracks were detected at the end of blast test. Cracks that formed after the fire exposure are depicted in red, whilst cracks that formed after the blast test are depicted in black. The LP0 test in which the blast load was applied without a high temperature exposure was characterized by the absence of cracks indicating as planned a linear elastic behaviour of the specimen. Looking at the HP0 specimen, characterized by a higher peak pressure and a higher impulse than specimen LP0 without fire exposure, a slight crack pattern both on the rear and front faces can be noted. Fire exposure induces quite severe damage in the specimens, revealed by the crack patterns shown in Fig. 13a-b-d-e-f. On the front face, the area in contact with the flame is clearly identifiable having a different colour and slight concrete spalling is visible in all the specimens exposed to fire (see grey regions in Fig. 13a-b-d-e-f). Fig. 14 shows the exposed surface of LP60 and HP120-2 specimens after the fire tests, as an example of each exposure time. In the pictures, both the area in contact with the flame and the region of concrete spalling can be easily recognized.

Radial cracks are always visible in all specimens exposed to fire. The radial cracks on the outer ring region of the slabs are mainly caused by the heating process that is directly applied to the central core of the slab. The thermal gradient between the central core and the external ring, because of the compatibility of the two regions, causes a circumferential tensile state of stress in the outer ring leading to the radial crack formation. In the specimens tested in HP conditions after fire exposure it is also possible to observe some circumferential cracks on the loaded surface (especially visible for HP60, Fig. 13d). This is due to the fact that, because the fire is applied only to the central region, the initial damage of the structure is not uniform along the radius but is more concentrated in the central heated region thus also creating a variation of the local sectional stiffness along the radius. The presence of an outer stiffer region affects the boundary condition thus also leading to the formation of radial tensile stresses on the loaded surface. In the case of a fire exposure time of 120 min, these cracks are less pronounced because the longer fire exposure leads to a more uniform distribution of the temperature and subsequently more uniform damage even along the radius.

The application of a blast load after the fire exposure has limited

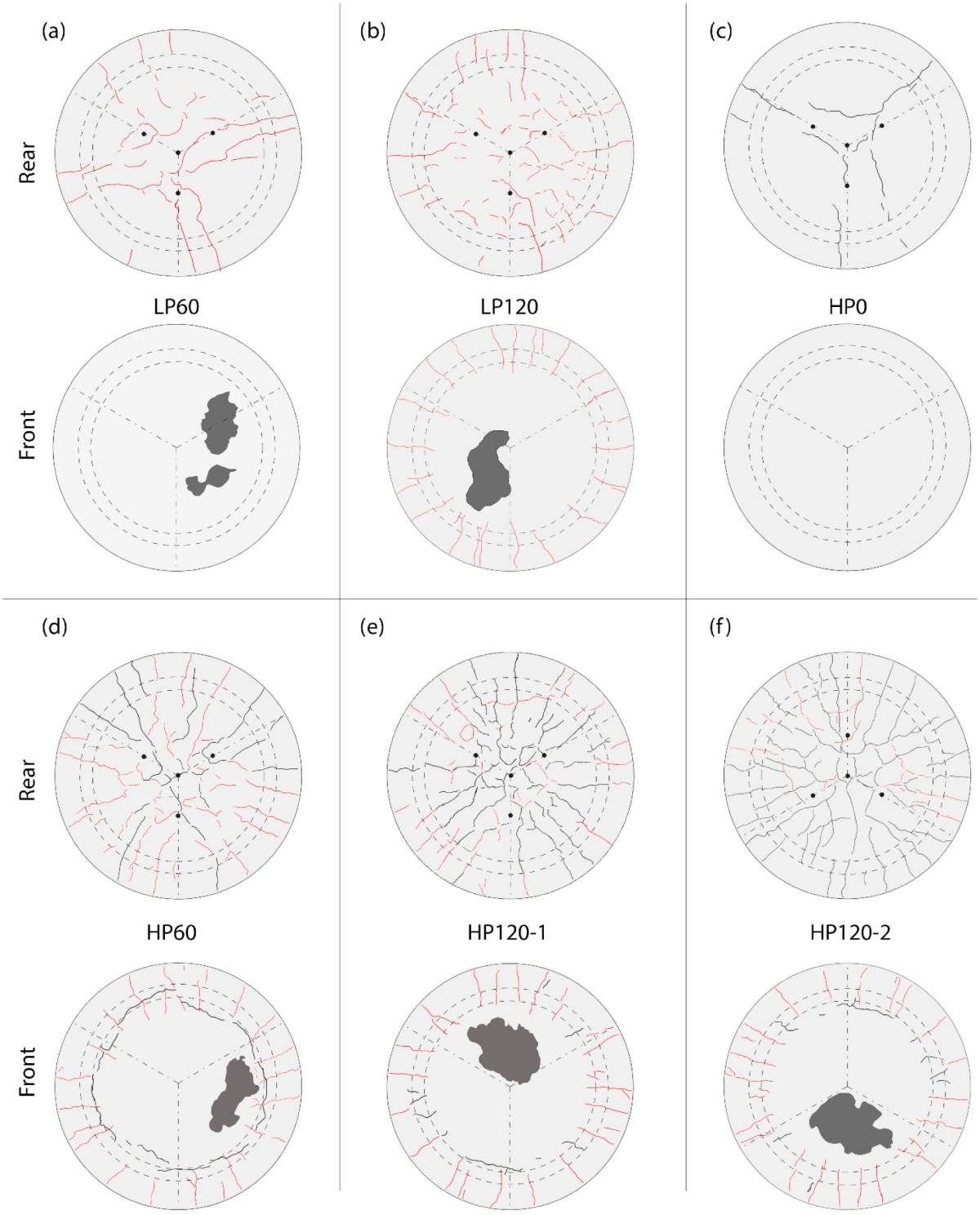

Fig. 13. Front and rear crack patterns for tests (a) LP60, (b) LP120, (c) HP0, (d) HP60, (e) HP120-1 and (f) HP120-2. Thermal and pressure cracks are indicated in red and in black respectively. (For interpretation of the references to colour in this figure legend, the reader is referred to the web version of this article.)

effects for specimens LP60 and LP120 since no new cracks were detected after the exposure to fire (Fig. 13a-b). A different trend can be observed in Fig. 13d-e-f for HP tests where the application of a blast load after the fire exposure produces further cracks in the specimens. It can be concluded that in LP tests, the main source of damage is the fire, while in HP tests both fire and blast contribute to the damage of the specimens, and the effect of blast is more amplified when a more severe fire exposure is applied.

Direct UPV measurements were carried out on the specimens before and after fire and blast loads. The aim of these measurements was to establish if, in case of fire and blast, the wave velocity decreases compared to the velocity in the pristine specimen, thus indicating that internal damage occurred in the specimen. Six points were monitored (Fig. 3) and average wave velocities are considered in the following discussion. Fig. 15 reports the average percentage reduction of wave velocity induced by fire and blast compared to the initial undamaged situation. In Fig. 15a, LP tests are examined first: effects of fire exposure are clearly visible leading to a wave velocity reduction of about 40% and

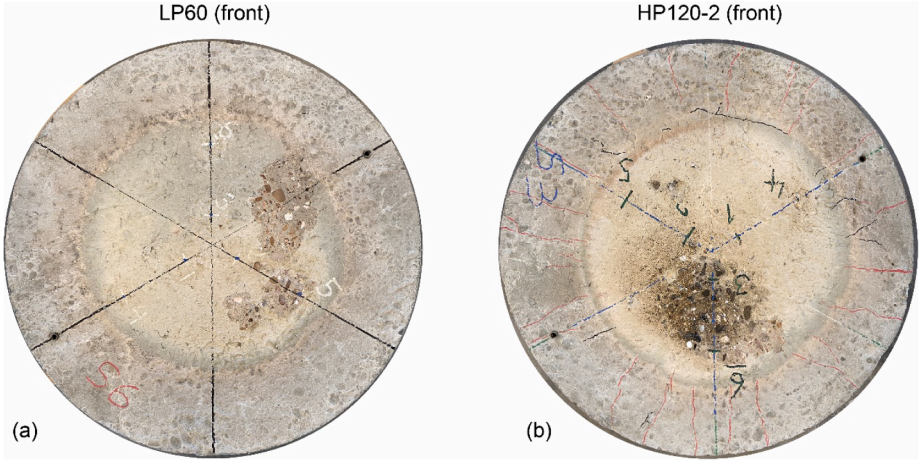

Fig. 14. Furnace flame footprint and spalling area for tests (a) LP60 and (b) HP120-2.

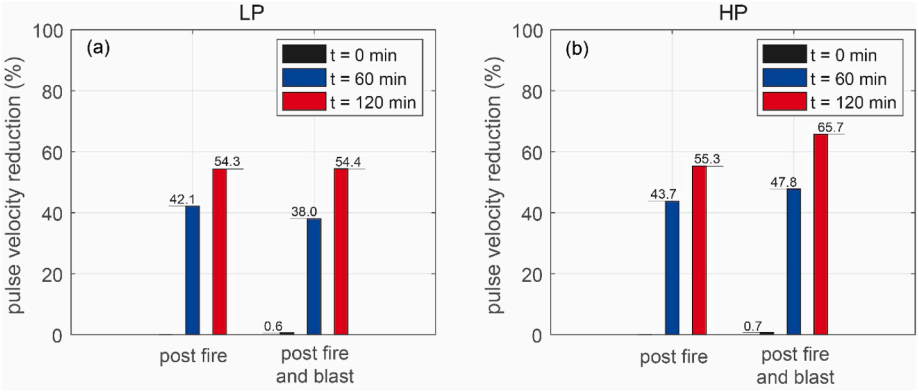

Fig. 15. Percentage reduction of direct ultrasonic pulse velocity results induced by fire and blast: (a) LP tests and (b) HP tests.

55% for fire exposure of 60 min and 120 min, respectively. In LP tests, the application of the blast load after the fire exposure does not significantly change the wave velocity, in line with the observed crack patterns discussed above. Looking at the HP tests, the wave velocity reduction due to fire exposure only is similar to that of LP tests. The application of a blast load in specimens already damaged by fire leads to a further reduction of the wave's velocity highlighting an increase in damage especially in specimens subjected to a fire exposure of 120 min. It should be emphasized that the cracks through the thickness of the specimen are not fully visible with direct UPV measurements. This justifies crack patterns on the specimens that are more severe than suggested by measurements with direct UPV.

5. Discussion

The experimental results presented in Section 4 are further analysed in this section using simplified tools, specifically: (i) an equivalent elastic single degree of freedom (SDOF) model and (ii) a linear elastic finite element (FE) model. Despite their simplicity, methods (i) and (ii) can be a useful tool to provide a deeper insight into the experimental results.

With reference to the equivalent SDOF model, the mass, the stiffness and the applied load of the RC slabs are replaced in the equation of motion with the equivalent values of a lumped mass–spring system. The principle of virtual displacement makes it possible to find the transformation coefficients that relate the equivalent mass, stiffness and load

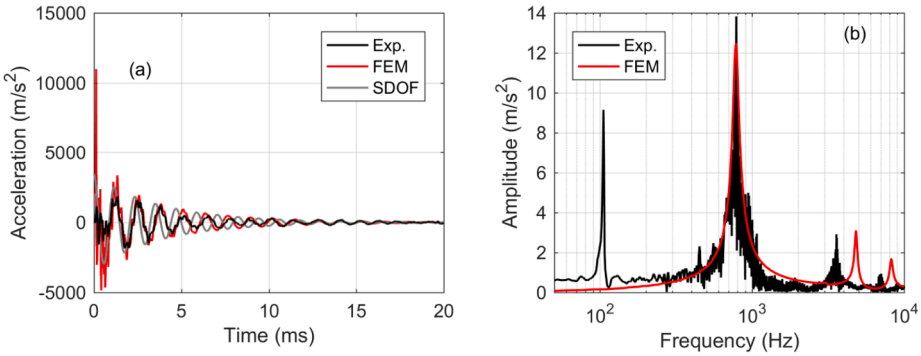

Fig. 16. Test LP0: a) time history acceleration A1 and b) frequency spectrum of signal A1.

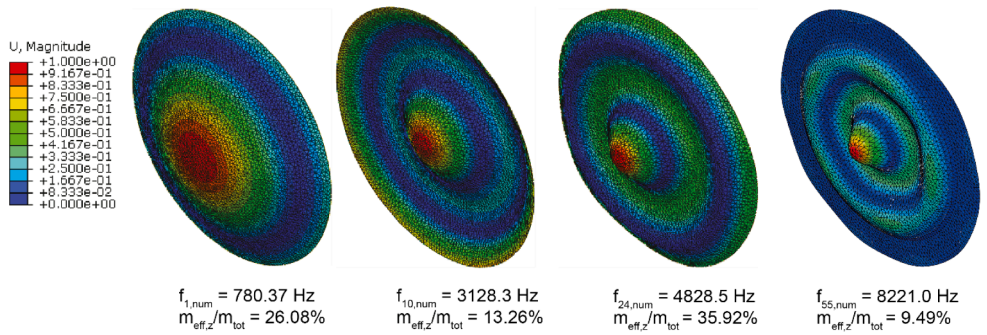

(a)

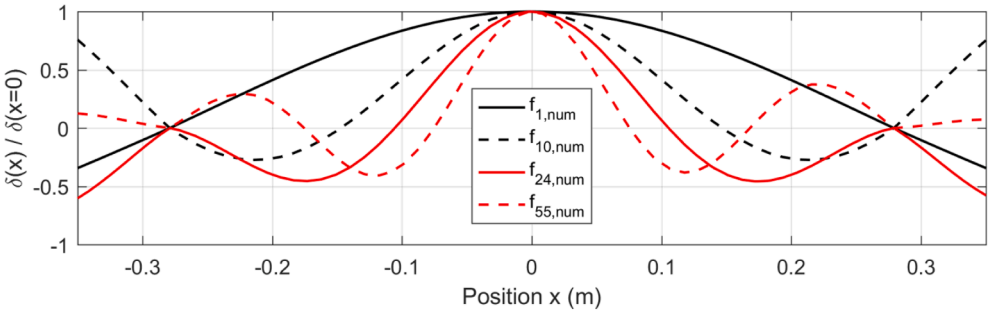

(b)

Fig. 17. First, tenth, twenty-fourth and fifty-fifth numerical modal shapes: (a) 3D views and (b) normalized displacement profiles along one diameter (U: normalized displacement amplitude).

in the SDOF system to their respective quantities in the actual slabs. The equivalent system has kinetic energy, strain energy and external work equal to the distributed system [48]. In calculating the transformation factors necessary to develop the equivalent SDOF model, a simplification was adopted: the loading area is extended up to the radius $r_1 = 275$ mm equal to the position of the support (see Fig. 7a). The equivalent system has a total diameter equal to the real specimen slab ($r_2 = 345$ mm). The elastic transformation factors used in this study are similar to those given in [49] for a simply supported plate; the exception is represented by the slab radius r_2 that does not coincide with the support radius r_1. The material parameters necessary to describe the SDOF model are the average values reported in Section 2.1.

With reference to the linear elastic FE model, this was built and processed in the Abaqus 6.14-5 environment [50], and consists of 7987 3-node triangular shell elements (element S3, average edge size 10 mm) connected through 4103 nodes. Boundary conditions and the blast load are applied according to the experimental set-up shown in Fig. 7. The elastic modulus of the concrete measured experimentally ($E \cong 28000$ MPa) was corrected by a factor of 1.15 to take into account the stiffening effect of the reinforcement following an homogenized approach for RC sections. The Young's modulus E, the Poisson's ratio ν and the density ρ adopted in the FE model are then assumed to be equal to $E = 32000$ MPa, $\nu = 0.2$ and $\rho = 2500$ kg/m^3. The finite element model, due to its simplicity, was used mainly for eigenfrequency analysis and for studying the dynamic response of the specimen that under blast loads did not show any damage (i.e. LP0). In this regard, specimen LP0 is an important reference to better understand the structural behaviour of all the other specimens.

Fig. 16a compares the central slab acceleration A1 recorded during the reference test LP0 with those obtained with the equivalent elastic SDOF model and with the FE model. The experimental acceleration is well reproduced by both simplified models. The frequency spectrum of the experimental signal A1 is compared with the numerical one (i.e. FE) in figure Fig. 16b. The first numerical frequency ($f_{1,num} = 780$ Hz) is

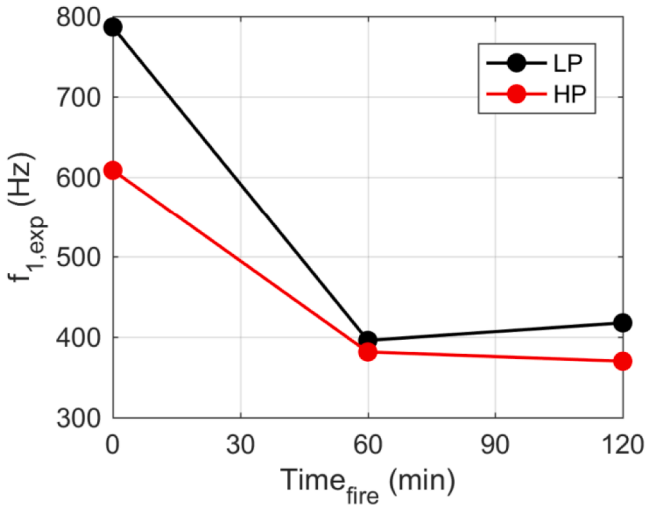

Fig. 18. Variation of the first experimental frequency $f_{1,exp}$ with the variation of the fire exposure time for the LP and HP tests.

almost identical to the experimental one ($f_{1,exp} = 787$ Hz); the second and third experimental peaks visible in Fig. 16b are overestimated by the FE model that results to be stiffer than the real slab. The SDOF model provides a first natural frequency equal to $f_{1,SDOF} = 812$ Hz that is slightly higher than the experimental one, but it can be considered a satisfactory prediction.

The experimental peak visible at the lowest frequency of about 100 Hz is not related to the slab response, but it depends on the shock tube's axial movement and should not be considered in the following discussion (see Section 4).

Fig. 17 illustrates the first four significant mode shapes of the FE model (Modes 1, 10, 24 and 55). These four mode shapes involve an out-

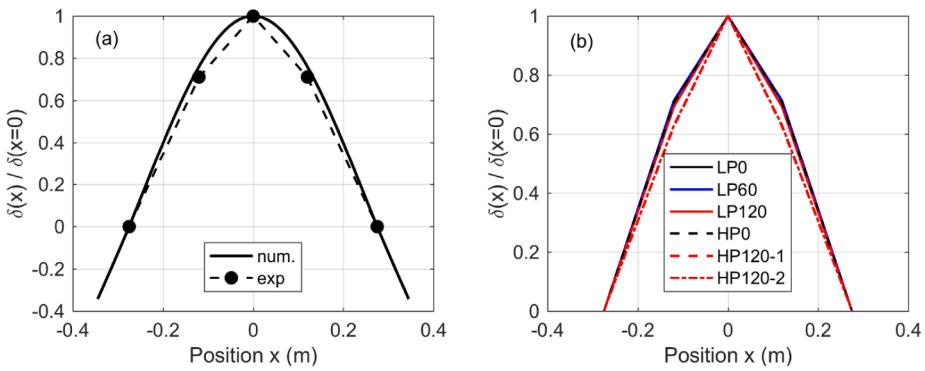

Fig. 19. (a) Comparison between experimental (LP0) and numerical first modal shape; (b) first modal shape derived from experimental data for all the specimens.

of-plane translation (the z direction) with an activation of the effective mass involved in z direction normalized with respect to the total mass of the model of 26%, 13%, 36% and 9% respectively. Mode shapes not shown in Fig. 17 involve negligible effective mass.

Given the good prediction of the slab's central acceleration provided by the SDOF system, it could be stated that the first mode of vibration mainly governs the slab's response. For this reason, a detailed analysis of this mode is discussed in the following.

By examining the frequency content of the signal A1 of all the specimens recorded during the blast tests it is also possible to establish the variation of the fundamental frequency $f_{1,exp}$ as the fire exposure time varies (Fig. 18). The variation of the fundamental frequency is directly correlated to the variation (reduction) of the stiffness of the specimen and is ultimately a measure of the accumulated damage. Looking at the LP tests and keeping in mind that test LP0 corresponds to an undamaged state, the fire exposure reduced the fundamental frequency by 50% providing a first frequency equal to about 400 Hz for a fire exposure time of both 60 and 120 min. Observing the HP tests, there is a reduction of the first frequency of 25% compared to the non-damaged situation for the blast effect only (test HP0). The exposure to fire further reduces the first frequency to values below 400 Hz for the HP120 tests, that corresponds to a first frequency reduction higher than 50% compared to the pristine specimen.

A Frequency Domain Decomposition (FDD) approach [51] was adopted to define the experimental modes of vibration of the slabs starting from the measurements of the accelerations during the tests. Fig. 19a compares the mode shape of the first mode of vibration provided by the eigenfrequency analysis with the mode shape obtained by the application of an FDD procedure to the experimental accelerations measured for test LP0. The figure represents the deformed shape of a diameter of the specimen considering a reference system placed in the centre of the slab (x = 0). Due to the small amount of accelerometers placed on the specimens, just the dotted points at x = 0 and x = ±0.12 m can be experimentally obtained, while the zero displacement condition is imposed at the support (x = ± 0.275 m). The figure shows good agreement between the experimental deformed shape and the numerical prediction; this comparison proves that the boundary conditions applied in the tests represent a simply supported condition well.

Fig. 19b presents the mode shape of the first mode of vibration for the different tests performed. The deformed shape of the first mode is almost identical for all the LP tests and for the HP0 test, while a slight difference can be observed for the two HP120 tests. The damage induced both by fire and by blast seems to have a limited effect on the first mode shape despite the change in mode frequency.

Damping is generally considered as a reliable indicator of damage in structures [52] and several studies have pointed out the effect of damage on damping [53–57]. Other investigations have even shown how cracks in RC structures could induce an increase of damping ratio [58] and that the change in damping is well correlated even to the crack depth [59].

The analysis of the decay of the acceleration peaks for all the experimental tests makes it possible to estimate the damping ratio ζ_{exp} and its variation compared to the undamaged situation (Fig. 20). Using the acceleration record ($\ddot{u}$) of the free vibration phase, the damping ratio was determined from:

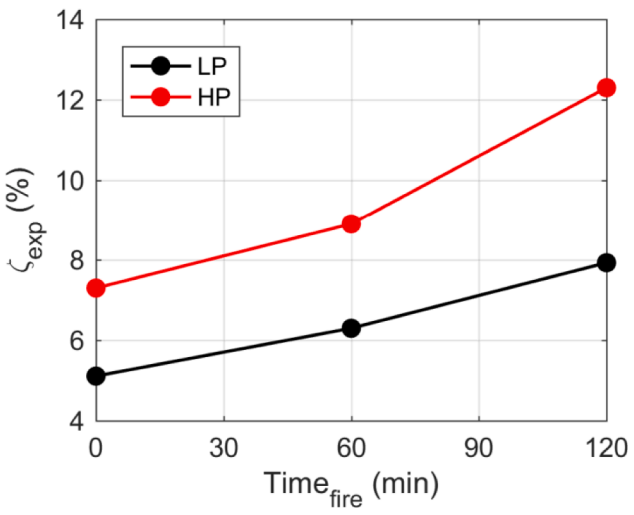

Fig. 20. Variation of damping ratio ζ_{exp} with the variation of the fire exposure time for the LP and HP tests.

$$\zeta_{exp} = \frac{1}{2\pi j} \ln \frac{\ddot{u}_i}{\ddot{u}_{i+j}} \tag{1}$$

where $\ddot{u}_i$ is the acceleration at the peak i and $\ddot{u}_{i+j}$ the acceleration at the peak $i+j$. Eq. (1) is valid for a lightly damped system. The damping ratio defined in Eq. (1) is a linear feature of damping and represents the extent of energy dissipation in the samples [52]. The presence of fire damage and/or cracks leads to larger energy dissipation and therefore to a larger damping ratio.

While the damping was approximately 5% for the LP0 specimen, the 60 min fire exposure (test LP60) increases the damping to 6%, and the 120 min fire exposure (LP120) further increases it to 7%. Looking at the HP tests, applying a higher peak pressure and impulse than the LP tests results in an increase of damping ratio equal to 7%. The combined effect of blast and fire leads to an increase in damping ratios of 9% and 12% for fire exposure times of 60 and 120 min, respectively. While the black curve in Fig. 20 can be seen as the exclusive contribution of the fire, the red curve represents the combined effect of blast and fire.

An ad-hoc subroutine was developed in a LabVIEW environment to derive reliable displacement measurements from the central acceleration signals A1 (Fig. 21). This subroutine consists of a double time integration of the acceleration applying a low pass filter at a frequency of 80 kHz before each time integration step.

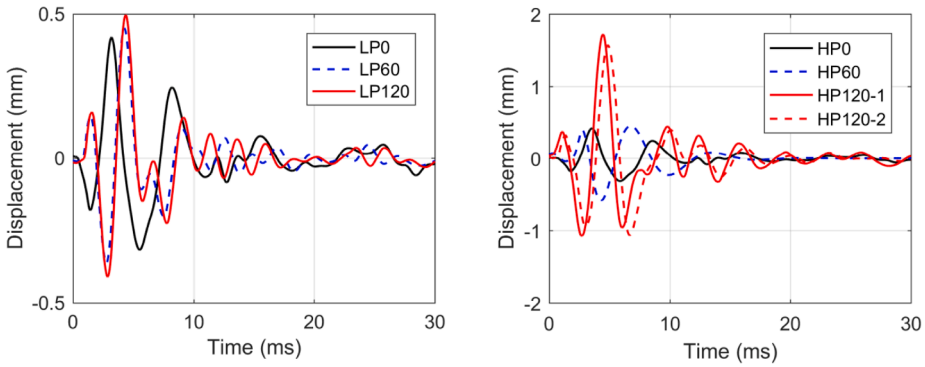

Fig. 21. Displacement-time history responses derived using a LabVIEW subroutine for (a) LP tests and (b) HP tests.

The effect of damage due to exposure to fire compared to the pristine specimen is clearly visible for both the LP (Fig. 21a) and HP (Fig. 21b) tests. In both figures the period elongation due to the combined effects of blast and fire is visible. For HP tests, the period elongation is also combined with an amplification of the maximum displacements with peaks that can be 3 times higher for specimens subjected to a fire exposure of 120 min compared to specimens without fire exposure.

6. Concluding remarks

In this study, the structural performance of reinforced concrete (RC) slabs subjected to combined fire and blast actions were investigated experimentally. The sequence of fire and blast was obtained using proper gas burner equipment and a shock tube device. Simplified numerical tools, namely (i) an equivalent elastic single degree of freedom (SDOF) model and (ii) a linear elastic finite element (FE) model were also used to provide a deeper insight into the experimental results. Based on this research, the following conclusions can be drawn:

- The shock tube used in the blast tests produced consistent and blast-like loading conditions characterized by high repeatability. Accelerometer recordings placed at 120° on the specimens confirm the planarity of the shock wave impacting the specimens.
- Test results pointed out the negligible role of the fluid–structure interaction in the cases investigated even when the samples were previously exposed to fire curves.
- Temperature evolutions, monitored using thermocouples embedded through the thickness of the slabs, show that the slabs reach temperatures between 250–600 °C and between 450–900 °C for fire exposure times of 60 and 120 min, respectively.
- Fire exposure causes cracks on both faces of the specimen; some of these cracks pass through the thickness. Limited concrete spalling was observed when the fire exposure was equal to 120 min. In LP tests, the subsequent application of blast loads after fire exposure does not significantly change the crack pattern. On the contrary, in HP tests the higher peak pressure and the higher impulse compared to LP tests induce new cracks in the specimens. This effect is maximized when the fire exposure time is higher (120 min).
- Fire exposure induces a pronounced decrease of strength and stiffness in the specimens, as pointed out by the analysis of (i) the crack patterns, (ii) the first frequency shift and (iii) the reduction of the wave velocity recorded using UPV measurements.
- The analysis of the frequency spectrum of the accelerometer signals shows a significant reduction of the slab's first frequency that was higher than 50% for HP120 tests compared to the pristine specimen.
- Experimental data makes it possible to estimate the evolution of the damping ratio as the fire exposure time varies and for different blast pressure levels. The damping ratios range from 5% for pristine specimen to 12% for HP120 tests, thus providing an indication of the damage accumulated by the slab specimens.
- The eigenvalue analysis on a simplified FE shell model provides a first numerical frequency that is in good agreement with the experimental one. This confirms the correctness of the set-up used during the shock tube tests that can be schematized as a simply supported condition. The simplified SDOF model also provides a fundamental frequency in good agreement with the experimental data.
- An ad-hoc subroutine developed in a LabVIEW environment made it possible to derive displacement estimations from the acceleration signals. The analysis of the specimens' central displacement shows that a greater exposure time to fire corresponds to greater displacement peaks in response to the blast loads. The maximum displacement values were 3 times higher for specimens subjected to a fire exposure of 120 min compared to specimens without fire exposure.
- The experimental data presented in this work is valuable in order to define a reliable benchmark for numerical models which, upon numerical upscaling, will be instrumental for the design of tunnels under exceptional load conditions, such as the combined action of fire and subsequent internal explosion.

Declaration of Competing Interest

The authors declare that they have no known competing financial interests or personal relationships that could have appeared to influence the work reported in this paper.

Acknowledgements

The work presented in this paper is part of an ongoing PhD study funded by the Norwegian Public Roads Administration as part of the Coastal Highway Route E39 project.

References

[1] Beard A, Carvel R. Handbook of tunnel fire safety. Second ed. ICE Publishing 2012.
[2] Kodur V, Naser M. Structural fire engineering. McGraw-Hill; 2020.
[3] Savov K, Lackner R, Mang HA. Stability assessment of shallow tunnels subjected to fire load. Fire Saf J 2005;40:745–63. https://doi.org/10.1016/j.firesaf.2005.07.004.
[4] Pichler C, Lackner R, Mang HA. Safety assessment of concrete tunnel linings under fire load. J Struct Eng 2006;132:961–9. https://doi.org/10.1061/(asce)0733-9445(2006)132:6(961).
[5] Yan ZG, Zhu HH, Woody JJ, Ding WQ. Full-scale fire tests of RC metro shield TBM tunnel linings. Constr Build Mater 2012;36:484–94. https://doi.org/10.1016/j.conbuildmat.2012.06.006.
[6] Lilliu G, Meda A. Nonlinear phased analysis of reinforced concrete tunnels under fire exposure. J Struct Fire Eng 2013;4:131–42. https://doi.org/10.1260/2040-2317.4.3.131.
[7] Felicetti R. Assessment methods of fire damages in concrete tunnel linings. Fire Technol 2013;49:509–29. https://doi.org/10.1007/s10694-011-0229-6.
[8] Wang F, Wang M, Huo J. The effects of the passive fire protection layer on the behavior of concrete tunnel linings: a field fire testing study. Tunn Undergr Sp Technol 2017;69:162–70. https://doi.org/10.1016/j.tust.2017.06.021.
[9] Sakkas K, Vagiokas N, Tsiamouras K, Mandalozis D, Benardos A, Nomikos P. In-situ fire test to assess tunnel lining fire resistance. Tunn Undergr Sp Technol 2019;85:368–74. https://doi.org/10.1016/j.tust.2019.01.002.

[10] Sun Z, Zhang Y, Yuan Y, Mang HA. Stability analysis of a fire-loaded shallow tunnel by means of a thermo-hydro-chemo-mechanical model and discontinuity layout optimization. Int J Numer Anal Methods Geomech 2019;43:2551–64. https://doi.org/10.1002/nag.2991.

[11] Lo Monte F, Felicetti R, Meda A, Bortolussi A. Explosive spalling in reinforced concrete tunnels exposed to fire: Experimental assessment and numerical modelling. In: Peila D, Viggiani G, Viggiani G, Celestino T, editors. Tunnels Undergr. Cities Eng. Innov. meet Archaeol. Archit. Art- Proc. WTC 2019 ITA-AITES World Tunn. Congr., CRC Press/Balkema 2019, 2519–26.

[12] Agrawal A, Kodur VKR. A novel experimental approach for evaluating residual capacity of fire damaged concrete members. Fire Technol 2020;56:715–35. https://doi.org/10.1007/s10694-019-00900-1.

[13] Stucchi R, Amberg F. A practical approach for tunnel fire verification. Struct Eng Int 2020;30:515–29. https://doi.org/10.1080/10168664.2020.1772697.

[14] EN 1991-1-2. Eurocode 1: Actions on structures—Part 1–2: General actions—Actions on structures exposed to fire. Brussels: 2004.

[15] EN 1992-1-2. Eurocode 2: Design of concrete structures— Part 1–2: General rules—Structural fire design. Brussel: 2004.

[16] Feldgun VR, Kochetkov AV, Karinski YS, Yankelevsky DZ. Internal blast loading in a buried lined tunnel. Int J Impact Eng 2008;35:172–83. https://doi.org/10.1016/j.ijimpeng.2007.01.001.

[17] Liu H. Dynamic analysis of subway structures under blast loading. Geotech Geol Eng 2009;27:699–711. https://doi.org/10.1007/s10706-009-9269-9.

[18] Liu H. Soil-structure interaction and failure of cast-iron subway tunnels subjected to medium internal blast loading. J Perform Constr Facil 2012;26:691–701. https://doi.org/10.1061/(asce)cf.1943-5509.0000292.

[19] Colombo M, Martinelli P, di Prisco M. Underground tunnels exposed to internal blast: Effect of the explosive source position. 711. 2016. doi:10.4028/www.scientific.net/KEM.711.852.

[20] Gao M, Zhang JY, Chen QS, Gao GY, Yang J, Li DY. An exact solution for three-dimensional (3D) dynamic response of a cylindrical lined tunnel in saturated soil to an internal blast load. Soil Dyn Earthq Eng 2016;90:32–7. https://doi.org/10.1016/j.soildyn.2016.08.031.

[21] Yu H, Wang Z, Yuan Y, Li W. Numerical analysis of internal blast effects on underground tunnel in soils. Struct Infrastruct Eng 2016;12:1090–105. https://doi.org/10.1080/15732479.2015.1077260.

[22] Zhao Y, Chu C, Vafeidis A, Li J. Vibration of a cylindrical tunnel under a centric point-source explosion. Shock Vib 2017;2017. https://doi.org/10.1155/2017/9152632.

[23] Kristoffersen M, Minoretti A, Børvik T. On the internal blast loading of submerged floating tunnels in concrete with circular and rectangular cross-sections. Eng Fail Anal 2019;103:462–80. https://doi.org/10.1016/j.engfailanal.2019.04.074.

[24] Prasanna R, Boominathan A. Finite-element studies on factors influencing the response of underground tunnels subjected to internal explosion. Int J Geomech 2020;20:04020089. https://doi.org/10.1061/(asce)gm.1943-5622.0001678.

[25] Goel MD, Verma S, Panchal S. Effect of internal blast on tunnel lining and surrounding soil. Indian Geotech J 2020. https://doi.org/10.1007/s40098-020-00451-1.

[26] Minoretti A, Xiang X, Johansen IL, Eidem M. The future of the tunnel crossing: the submerged floating tube bridge. Struct Eng Int 2020;30:493–7. https://doi.org/10.1080/10168664.2020.1775165.

[27] Kakogiannis D, Pascualena F, Reymen B, Pyl L, Ndambi JM, Segers E, et al. Blast performance of reinforced concrete hollow core slabs in combination with fire: Numerical and experimental assessment. Fire Saf J 2013;57:69–82. https://doi.org/10.1016/j.firesaf.2012.10.027.

[28] Pascualena F, Ndambi J, Reymen B, Desmet B, Segers E, Vantomme J. Blast performance of concrete slabs in combination with fire. Proc. 8th Int. Conf. Struct. Dyn. EURODYN 2011, Leuven Belgium: 2011, 3310–7.

[29] Ruan Z, Chen L, Fang Q. Numerical investigation into dynamic responses of RC columns subjected for fire and blast. J Loss Prev Process Ind 2015;34:10–21. https://doi.org/10.1016/j.jlp.2015.01.009.

[30] Zhai C, Chen L, Xiang H, Fang Q. Experimental and numerical investigation into RC beams subjected to blast after exposure to fire. Int J Impact Eng 2016;97:29–45. https://doi.org/10.1016/j.ijimpeng.2016.06.004.

[31] Zhang Q, Wang WY, Bai SS, Tan YH. Response analysis of tunnel lining structure under impact and fire loading. Adv Mech Eng 2019;11:1–6. https://doi.org/10.1177/1687814019834473.

[32] Colombo M, Martinelli P, di Prisco M. A design approach for tunnels exposed to blast and fire. Struct Concr 2015;16:262–72. https://doi.org/10.1002/suco.201400052.

[33] Colombo M, di Prisco M, Martinelli P. A new shock tube facility for tunnel safety. Exp Mech 2011;51:1143–54. https://doi.org/10.1007/s11340-010-9430-7.

[34] Arano A, Colombo M, Martinelli P, Øverli JA, Hendriks MA, Kanstad T, et al. Material characterization approach for modelling high-strength concrete after cooling from elevated temperatures. J Mater Civ Eng 2021;33:04021086. https://doi.org/10.1061/(ASCE)MT.1943-5533.0003694.

[35] ITA-AITES. Guidelines for structural fire resistance for road tunnels. 2004.

[36] ISO 1920-10:2010. Testing of concrete - Part 10: Determination of static modulus of elasticity in compression. 2010.

[37] ISO 15630-1:2019. Steel for the reinforcement and prestressing of concrete - Test methods - Part 1: Reinforcing bars, rods and wire. 2019.

[38] Timoshenko S, Woinowsky-Krieger S. Theory of plates and shells. New York: McGraw-Hill; 1959.

[39] Johansen K. Yield-line theory. London: Cement and Concrete Association; 1962.

[40] Bungey J, Millard S, Grantham M. Testing of concrete in structures. 4th ed. London: Taylor and Francis; 2006. https://doi.org/10.1201/9781482264685.

[41] Ritzel D, Thibault P. Development of an efficient low-cost blast tube facility. Tenth Int. Symp. Mil. Appl. Blast Simul. (MABS 10), Freiburg, Germany: 1987.

[42] NATO-AEP-25. Nuclear Blast and Thermal Test Methods and Procedures. NATO Allied Engineering Publication; 1995.

[43] Toutlemonde F, Rossi P, Boulay C, Gourraud C, Guedon D. Dynamic behaviour of concrete: tests of slabs with a shock tube. Mater Struct 1995;28:293–8. https://doi.org/10.1007/BF02473264.

[44] Kristoffersen M, Pettersen JE, Aune V, Børvik T. Experimental and numerical studies on the structural response of normal strength concrete slabs subjected to blast loading. Eng Struct 2018;174:242–55. https://doi.org/10.1016/j.engstruct.2018.07.022.

[45] Colombo M, Martinelli P, di Prisco M. Layered high-performance concrete plates interacting with granular soil under blast loads: An experimental investigation. Eur J Environ Civ Eng 2013;17:1002–25. https://doi.org/10.1080/19648189.2013.841595.

[46] Colombo M, Martinelli P, di Prisco M. On the blast resistance of high performance tunnel segments. Mater Struct Constr 2016;49:117–31. https://doi.org/10.1617/s11527-014-0480-7.

[47] Andreotti R, Colombo M, Guardone A, Martinelli P, Riganti G, di Prisco M. Performance of a shock tube facility for impact response of structures. Int J Non Linear Mech 2015;72:262–72. https://doi.org/10.1016/j.ijnonlinmec.2015.02.010.

[48] Biggs J. Introduction to structural dynamics. New York: McGraw-Hill; 1964.

[49] Colombo M, Martinelli P. Pressure-impulse diagrams for RC and FRC circular plates under blast loads. Eur J Environ Civ Eng 2012;16:837–62. https://doi.org/10.1080/19648189.2012.675149.

[50] Dassault Systèmes. Abaqus analysis user's manual - version 6.14 2016.

[51] Brincker R, Zhang L, Andersen P. Modal identification from ambient responses using frequency domain decomposition. Proc. Int. Modal Anal. Conf. - IMAC 2000: 625–30.

[52] Cao MS, Sha GG, Gao YF, Ostachowicz W. Structural damage identification using damping: A compendium of uses and features. Smart Mater Struct 2017;26:043001. https://doi.org/10.1088/1361-665X/aa550a.

[53] Kennedy J, Grace N. Prestressed continuous composite bridges under dynamic load. J Struct Eng (United States) 1990;116:1660–78.

[54] Rezaee M, Hassannejad R. Free vibration analysis of simply supported beam with breathing crack using perturbation method. Acta Mech Solida Sin 2010;23:459–70. https://doi.org/10.1016/S0894-9166(10)60048-1.

[55] Chandra R, Singh SP, Gupta K. A study of damping in fiber-reinforced composites. J Sound Vib 2003;262:475–96. https://doi.org/10.1016/S0022-460X(03)00107-X.

[56] Kyriazoglou C, Guild FJ. Quantifying the effect of homogeneous and localized damage mechanisms on the damping properties of damaged GFRP and CFRP continuous and woven composite laminates-an FEA approach. Compos Part A Appl Sci Manuf 2005;36:367–79. https://doi.org/10.1016/j.compositesa.2004.06.037.

[57] Birman V, Byrd LW. Effect of matrix cracks on damping in unidirectional and cross-ply ceramic matrix composites. J Compos Mater 2002;36:1859–77. https://doi.org/10.1177/0021998302036015247.

[58] Daneshjoo F, Gharighoran A. Experimental and theoretical dynamic system identification of damaged RC beams. Electron J Struct Eng 2008;8:29–39.

[59] Panteliou SD, Chondros TG, Argyrakis VC, Dimarogonas AD. Damping factor as an indicator of crack severity. J Sound Vib 2001;241:235–45. https://doi.org/10.1006/jsvi.2000.3299.